

New kinematic map of the Milky Way bulge[★]

C. Quezada^{1,2,★★}, M. Zoccali^{1,2}, E. Valenti^{3,4}, A. Rojas Arriagada^{2,5,6,7}, A. Renzini⁸, O. A. Gonzalez⁹,
A. Mucciarelli^{10,11}, M. Rejkuba³, F. Surot¹², and A. Valenzuela Navarro^{1,2}

¹ Instituto de Astrofísica, Pontificia Universidad Católica de Chile, Av. Vicuña Mackenna 4860, 782-0436 Macul, Santiago, Chile

² Millennium Institute of Astrophysics, Av. Vicuña Mackenna 4860, 82-0436 Macul, Santiago, Chile

³ European Southern Observatory, Karl Schwarzschild-Straße 2, 85748 Garching bei München, Germany

⁴ Excellence Cluster ORIGINS, Boltzmann-Straße 2, 85748 Garching bei München, Germany

⁵ Departamento de Física, Universidad de Santiago de Chile, Av. Victor Jara 3659, Santiago, Chile

⁶ Núcleo Milenio ERIS, ANID, Chile

⁷ Center for Interdisciplinary Research in Astrophysics and Space Exploration (CIRAS), Universidad de Santiago de Chile, Santiago, Chile

⁸ INAF – Osservatorio Astronomico di Padova, Vicolo dell’Osservatorio 5, 35122 Padova, Italy

⁹ UK Astronomy Technology Centre, Royal Observatory, Blackford Hill, Edinburgh EH9 3HJ, UK

¹⁰ Dipartimento di Fisica & Astronomia “Augusto Righi” – Università degli Studi di Bologna, Via Piero Gobetti 93/2, 40129 Bologna, Italy

¹¹ INAF – Osservatorio di Astrofisica e Scienza dello Spazio di Bologna, Via Gobetti 93/3, 40129 Bologna, Italy

¹² Instituto de Astrofísica de Canarias, Calle Vía Láctea s/n, E-38206 La Laguna, Tenerife, Spain

Received 7 May 2025 / Accepted 19 August 2025

ABSTRACT

Context. The kinematics of the Milky Way bulge is known to be complex, reflecting the presence of multiple stellar components with distinct chemical and spatial properties. In particular, the bulge hosts a bar structure exhibiting cylindrical rotation, and a central velocity dispersion peak extending vertically along the Galactic latitude. However, due to severe extinction and crowding, observational constraints near the Galactic plane are sparse, underscoring the need for additional data to improve the completeness and accuracy of existing kinematic maps, and enabling robust comparison with dynamical models.

Aims. This work aimed to refine the existing analytical models of the Galactic bulge kinematics by improving constraints in the innermost regions. We present updated maps of the mean velocity and velocity dispersion by incorporating new data near the Galactic plane.

Methods. We combined radial velocity measurements from the GIBS and APOGEE surveys with both previously published and newly acquired MUSE observations. A custom-developed Python-based tool, PHOTfun, was used to extract spectra from MUSE datacubes using PSF photometry based on DAOPHOT-II, with an integrated GUI for usability. The method included a dedicated extension, PHOTcube, optimized for IFU datacubes. We applied Markov Chain Monte Carlo techniques to identify and correct for foreground contamination and to derive new analytical fits for the velocity and velocity dispersion distributions. Our analysis included nine new MUSE fields located close to the Galactic plane, bringing the total number of mapped fields to 57 including 23 000 individual RV measured.

Results. The updated kinematic maps confirm the cylindrical rotation of the bulge and reveal a more boxy morphology in the velocity dispersion distribution, while preserving a well-defined central peak. The PHOTfun software, designed for flexible PSF photometry and spectral extraction from IFU data, is publicly available via pip for the community.

Key words. methods: data analysis – techniques: imaging spectroscopy – techniques: photometric – techniques: radial velocities – Galaxy: bulge – Galaxy: kinematics and dynamics

1. Introduction

One of the common massive components in galaxies is the bulge, typically defined as the central region where a substantial fraction of the stellar mass is concentrated, resulting in a high surface brightness. Moreover, bulges generally form alongside their host galaxies, retaining traces of their complete evolutionary history.

In the bulge, the spatial distribution of stars is a consequence of the kinematical evolution during the galaxy formation history. An example is the so-called classical or spheroidal bulges

seen in some spiral galaxies, which are pressure-supported structures traditionally believed to have formed through early, violent mergers (Kauffmann et al. 1993; Hopkins et al. 2010; Garrison-Kimmel et al. 2018). Another example is the elongated bar often seen crossing the center of spiral galaxies.

This feature is believed to arise from the secular evolution of the galactic disk, in which kinematic instabilities in stellar orbits give rise to a barred structure. Subsequent buckling instabilities may occur, resulting in a boxy or peanut-shaped bulge (Patsis et al. 2002; Athanassoula 2005; Shen et al. 2010; Portail et al. 2015).

Besides mergers and orbital instabilities, in more recent years a third option has gained momentum, one in which the formation of bulges in high-redshift galaxies can result from the inward

[★] Based on observations taken at the ESO Very Large Telescope with the MUSE instrument under program IDs 101.B-0381(A) (SM; PI: Zoccali), and 101.D-0363(A) (SM; PI: Minniti).

^{★★} Corresponding author: ciquezada@uc.cl

migration of gas from the disk, then feeding a star-forming bulge. In one option of this scenario, giant star-forming clumps can form in the gas-rich disk, which would then migrate and coalesce toward the center (for example, [Immeli et al. 2004](#); [Carollo et al. 2007](#); [Elmegreen et al. 2008](#); [Genzel et al. 2008](#); [Bournaud et al. 2009](#)) Besides clump formation and migration, the possibility of overall violent disk instabilities has also been proposed, which would lead to the central accumulation of large amounts of gas, then rapidly depleted by star formation and winds (for example, [Dekel & Burkert 2014](#); [Tacchella et al. 2016](#)) Relatively smooth radial gas flows have been detected in high-redshift galaxies ([Genzel et al. 2023](#)), possibly driven by bars or spiral arms, then contributing to bulge growth via in situ star formation. In all such versions, rotating bulges form rapidly being fed by the disk, in a gas-rich, highly dissipative environment, for which ALMA spatially resolved observations have shown plausible examples among redshift ~ 2 galaxies (for example, [Tadaki et al. 2017](#)).

In the Milky Way (MW), the bulge is the region within a radius of ≈ 3.5 kpc around the center. This central component concentrates a substantial fraction, $\sim 30\%$, of the total stellar mass of the Galaxy ([Valenti et al. 2016](#); [Portail et al. 2017](#); [Simion et al. 2017](#); [Zoccali & Valenti 2024](#)). It is one of the oldest galactic components (for instance, ≈ 10 Gyr), hosting some of the first stars formed in the Galaxy ([Tumlinson 2010](#); [Clarkson et al. 2011](#); [Bensby et al. 2017](#); [Renzini et al. 2018](#)). The bulge lies only about 5–8 kpc from us, making it exceptionally well resolved in stars as faint as the main sequence; hence, it offers us a unique opportunity to study this crucial component for understanding the MW formation.

The elongated stellar orbits characteristic of a bar, coupled with a spheroidal spatial distribution, constitute distinct kinematic and structural signatures of the bulge formation process, as reflected in the line of sight velocity distributions. Consequently, constructing detailed maps of radial velocity (RV) and RV dispersion (σ_{RV}) serves as a powerful diagnostic tool for constraining the formation history of the Galactic bulge. ([Zoccali et al. 2014](#); [Molaiezhad et al. 2016](#); [Simion et al. 2017](#); [Debattista et al. 2017, 2019](#)). Several spectroscopic surveys that have mapped the chemistry and kinematics of the MW bulge (for example, BRAVA: [Rich et al. \(2007\)](#); [Kunder et al. \(2012\)](#), ARGOS: [Freeman et al. \(2013\)](#), Gaia ESO: [Rojas-Arriagada et al. \(2014\)](#), GIBS: [Zoccali et al. \(2014\)](#), APOGEE: [Rojas-Arriagada et al. \(2020\)](#)) have revealed that it hosts at least two stellar populations with distinct spatial distribution, chemical composition, and kinematics. Specifically, while metal-rich stars trace the barred, boxy/peanut structure, the metal-poor population follows a more spheroidal distribution ([Babusiaux et al. 2010](#); [Zoccali et al. 2017](#); [Queiroz et al. 2020](#); [Lim et al. 2021](#)). Mapping the global kinematics of the MW bulge offers a well resolved benchmark for comparison with more distant galaxies, where individual stars cannot be distinguished. Moreover, the presence of multiple structural components provides valuable insights into more intricate galaxy formation pathways.

Using measurements from the GIBS survey, [Zoccali et al. \(2014, hereafter Z14\)](#) presented the first analytical maps of RV and σ_{RV} of the MW bulge in the region $|l, b| \leq 10^\circ$. These maps, expressed as functions of Galactic coordinates, were derived by interpolating data from 30 observed fields across the entire bulge region, assuming two-folds symmetry. The GIBS fields, each containing between 100 and 400 red clump (RC) giants, extend as close as ≈ 2 degrees from the Galactic plane (see Fig. 1). The RV map revealed clear signature of cylindrical rotation – namely, stars at different latitudes exhibit similar RV values at a given

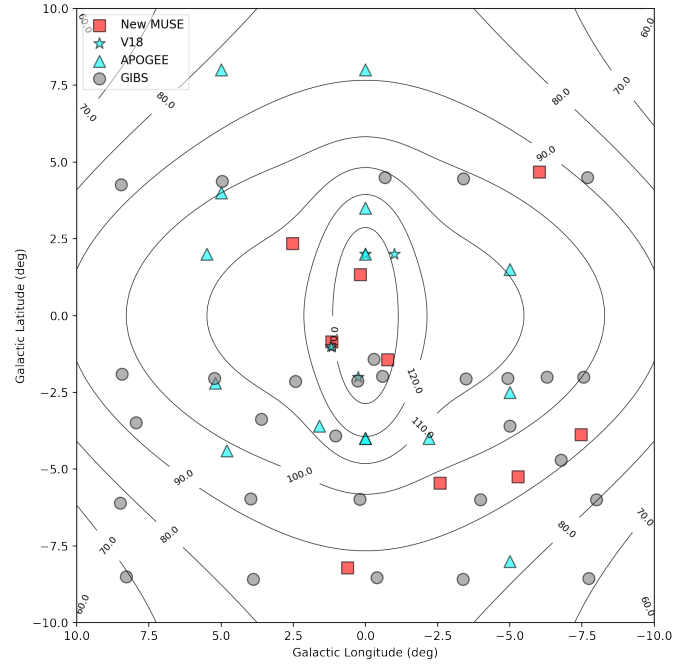


Fig. 1. Spatial distribution in Galactic coordinates of the global spectroscopic sample considered in this study compared to the σ_{RV} contours (solid lines) of the Z14 map. The GIBS fields used to derive the map of Z14 are marked as gray circles, while the cyan symbols refer to the additional fields used in this work to derive new map. Specifically, the new MUSE fields (red squares), the APOGEE fields (cyan triangles), and the V18 fields (cyan stars).

longitude, similar results also found by [Howard et al. \(2009\)](#); [Ness et al. \(2013\)](#) among other authors. In contrast, the σ_{RV} map showed a prominent central peak, reaching values around 140 km/s and extending along 2 degrees from the center, which is equivalent to be confined within a radius of ≈ 280 pc, considering each degree as 140 pc assuming a distance to the center of 8 kpc. Accurately characterizing this central peak, particularly in terms of its spatial extension, is crucial, as it may be linked either to a central stellar density enhancement ([Valenti et al. 2016](#)) that could be related to an inner component like the nuclear star cluster – which hosts a total stellar mass of $\sim 3 \times 10^7 M_\odot$ in a small radius of ~ 4 pc, see [Neumayer et al. \(2020\)](#) for further details – or to the presence of elongated orbits along the line of sight, often referred to as anisotropy of the orbits ([Simion et al. 2021](#)). However, due to the challenges posed by high extinction and stellar crowding, the innermost regions near the Galactic plane remain poorly constrained. To address this limitation, [Valenti et al. \(2018, hereafter V18\)](#) supplemented the GIBS kinematic maps with four additional inner fields ($|b| \sim 2^\circ$) observed with the integral field unit (IFU) spectrograph MUSE ([Bacon et al. 2010](#)) at the ESO Very Large Telescope (VLT). Despite the low resolution of MUSE ($R \approx 3000$), the RV was measurable by means of the prominent absorption lines of the Calcium II triplet (hereafter CaT; an example of these lines around wavelength 8600 \AA is shown in Fig. 3). These new observations, based on significantly larger stellar sample (for instance, ≈ 500 – 1200 per field), confirmed both the vertical extent of the σ_{RV} peak at positive latitudes and its symmetry with respect to the Galactic plane.

To further constrain the kinematic properties of the stellar population in the inner bulge, we present an analysis of nine

newly observed fields using the MUSE spectrograph, employing similar methodology as in V18. In addition, by integrating archival data from V18, GIBS and APOGEE, we update the existing maps of mean RV and σ_{RV} maps, deriving revised analytical expressions as functions of Galactic coordinates. Finally, the new MUSE data were processed using the PHOTfun code, which performs standard Point Spread Function (PSF) photometry on the monochromatic images obtained from the MUSE datacubes. Its PHOTcube extension enables the extraction of stellar spectra by concatenating the flux measurements (derived from the magnitude conversion) of each detected source across the datacube. While PHOTfun was originally designed for PSF photometry on arbitrary image sets, the integration of PHOTcube extends its functionality to IFU datacubes, facilitating simultaneous photometric and spectroscopic analysis. The complete toolkit is released as unified software suite under the name PHOTfun.

2. The spectroscopic sample

The kinematic maps presented in this study were derived by combining several different spectroscopic datasets, some of them analyzed here for the first time, and some other already published. In total, the maps are based upon $\sim 23\,000$ stars, spread across 57 bulge fields. We describe each datasets here below.

MUSE-inner. These are three fields located within ~ 150 pc from the Galactic center, observed within ESO proposal 101.B-0381 (P.I. Zoccali, M). The original purpose of these data was to characterize the σ_{RV} peak, in the inner bulge, presented for the first time by Z14. The reduction of these data are described here for the first time, in Sect. 3. Table 1 lists the Galactic coordinates, the exposure time, the image quality and extinction (Surot et al. 2020) of all MUSE fields used in this work.

MUSE-outer. Six additional fields were observed further away from the Galactic center, within ESO proposal 101.D-0363 (P.I. Minniti, D). The fields were centered at the coordinates of candidate new globular clusters, later discarded by Gran et al. (2019). Therefore, they sample bulge field (and foreground disk) stars, and had much shorter exposure times. The reduction and analysis of these data are also described here for the first time (Sect. 3).

As these datasets (MUSE-inner and -outer) are being for the first time analyzed, we refer to them as the new MUSE data. Each field name follows the same codename convention as the GIBS data, based on the Galactic coordinates; for example, ($l^\circ=0.2$, $b^\circ=1.3$) is labeled as p0.2p1.3.

MUSE-V18. These are the four fields in the inner bulge, acquired within ESO proposal 99.B-0311 and discussed in V18. We use here directly the RV measurements obtained in that paper.

GIBS data. The main goal of the present work is to update the kinematic maps presented by Z14. Therefore, we included here all the data from that paper. They consist in RV measurements for a sample of ~ 5000 RC stars only, spread across 30 fields, mostly at negative latitudes. The spectra were obtained with the FLAMES-GIRAFFE¹ spectrograph (Pasquini et al. 2000), at resolution $R\sim 6500$, and were centered on the infrared CaT region at ~ 8500 Å.

¹ Based on observations taken with ESO telescopes at the La Silla Paranal Observatory under ESO programme IDs 187.B-909 and 089.B-0830.

Table 1. Parameters of the new MUSE observations.

Field	l [deg]	b [deg]	Exp. time [s]	FWHM [']	E(J-K) mag
p0.2p1.3	0.19	1.30	6×1100	0.97	0.920
	0.18	1.34	6×1000	0.76	0.885
	0.19	1.35	6×1000	0.77	0.998
m0.7m1.4	-0.75	-1.42	6×1000	0.80	0.991
	-0.77	-1.43	6×1100	0.92	1.019
	-0.79	-1.44	6×1020	1.00	0.996
p1.2m0.9	1.17	-0.87	6×1000	0.92	0.851
	1.16	-0.85	6×1000	0.85	0.878
	1.17	-0.84	1×1000	1.02	0.744
m5m5	-5.28	-5.25	3×1035	0.81	0.217
p1m8	0.62	-8.22	3×700	0.65	0.102
p3p2	2.53	2.34	3×1035	0.61	0.623
m7m4	-7.46	-3.87	3×1035	0.79	0.472
m3m5	-2.58	-5.46	3×1035	0.59	0.255
m6p5	-6.02	4.68	3×1030	0.72	0.341

Notes. Columns list names, galactic coordinates, exposure times, image quality as measured on the FoV images, reddening from Surot et al. (2020).

APOGEE data. The APOGEE survey (Majewski et al. 2017) targeted red giant stars across the whole MW. For the present study, we selected bona-fide bulge stars from the DR17 catalog (Abdurro'uf et al. 2022) by following the prescriptions of Rojas-Arriagada et al. (2020). Briefly, we retained all M giants in the region between $|l| \leq 10^\circ$ and $|b| \leq 10^\circ$, with spectro-photometric distance within 3.5 kpc from the Galactic center. Additionally, to account for metallicity bias due to the survey selection function and to the limited sampling of the models grid of the APOGEE pipeline, we further excluded all stars with $\log(g) \geq 2.2$ (see Sect. 3.1 in Rojas-Arriagada et al. 2020). The so-derived APOGEE catalog has been used to further select 14 bulge regions with a relatively high target density (for example, ≥ 100 stars per circular area of 1 degree of radius), and derived a RV and σ_{RV} for each of them.

Finally, it is worth stressing that the selection of all spectroscopic fields, both new and previously published, aims at enhancing the spatial sampling in the region between $|l| \leq 10^\circ$ and $|b| \leq 10^\circ$, and hence enabling a more precise constraint on the existing map, especially in the innermost regions (see Fig. 1).

3. Reduction and analysis of the new MUSE data

For the new datasets, MUSE-inner and MUSE-outer, we provide here a detailed description of the observations, data reduction, spectrum extraction and RV measurements.

3.1. Observations and data reduction

As part of an ongoing project aimed at probing the kinematics and chemistry of the stellar population of the inner Galactic bulge, we have collected deep MUSE observations of three fields (for instance, p0.2p1.3, m0.7m1.4, p1.2m0.9) within ~ 150 pc from the Galactic center. We have carried out multiple MUSE adjacent pointing leading to a mapped area of about 3 arcmin² per field, and performed multiple visits to enable the detection

and RV measurement of dwarfs ~ 1 mag fainter than the bulge main-sequence turnoff (for instance, $I \sim 19$), with signal-to-noise (SNR) ≥ 12 . Six additional fields, consisting of just one pointing each, have been found in the ESO/MUSE archive as part of a program aimed at searching for obscure bulge clusters, and have been included in our sample to improve the spatial coverage across the bulge (see Table 1).

MUSE (Bacon et al. 2010) consists of 24 identical IFU that – when used as in our case in Wide Field Mode (WFM) – together sample a nearly contiguous area of 1 arcmin², with a spatial resolution of 0.2''/px. The observations of all fields have been combined with the Ground Layer Adaptive Optics mode (for instance, WFM-AO) of the VLT Adaptive Optics Facility (Arsenault et al. 2008) through the GALACSI AO module (Ströbele et al. 2012), which acts as seeing enhancer. By using the so-called Nominal setup (for instance, WFM-AO-N), the resulting spectra span mostly over the whole optical range – for instance, from 4800 Å to 9300 Å, with a gap 5820–5970 Å due to the Na Notch filter blocking the emission from the lasers – with a resolution of $R \sim 3100$ at 8000 Å, and a sampling of 1.25 Å. For all the fields, similar observing strategy but different total integration time (see Table 1) has been used: a combination of on-target sub-exposures, taken with a small offsets pattern (for instance, $\sim 1.5''$) and 90° rotations to optimize the cosmic rays rejection and obtaining a uniform combined dataset in terms of noise properties.

Raw data processing has been carried out by using the MUSE pipeline (Weilbacher et al. 2020). As first step, the pipeline produces the master calibrations needed to account for the instrumental effects (for example, bias, flats, arc lamps, line spread function, illumination, geometrical distortion and response curve for flux calibration). Subsequently, the correction by using the master calibrations is performed for each exposure of each individual IFU, and a pixel table containing the processed data coming from all the 24 IFUs is created. For each MUSE pointing, a final datacube is then obtained by combining together the pixel tables corresponding to all the available exposures. Additionally, we have used the pipeline option of producing the so-called field-of-view (FoV) images by convolving the MUSE datacube with the transmission curve of various filters. For this work we produced FoV images in V-Johnson, R-Cousins, and I-Cousins, as well as the white light FoV image covering the whole spectral range.

3.2. Software release: PHOTfun and PHOTcube

PHOTfun is a Python package developed in the context of this work to facilitate PSF photometry tasks based on the well established software packages DAOPHOT-II and ALLSTAR (Stetson 1987). It also includes a dedicated extension, PHOTcube, specifically designed for spectral extraction from IFU datacubes. In crowded stellar fields, spectral extraction requires PSF-based photometry to accurately deblend sources. While previous tools such as PampelMUSE (Kamann et al. 2013) implement similar functionality, they present key limitations: (i) they require a predefined list of targets for spectral extraction, (ii) they do not allow interactive selection of the stars used for PSF modeling, and (iii) they are less effective at subtracting sky artifacts compared to DAOPHOT-II-based methods. The PHOTfun package consists of two main components: a graphical user interface (GUI) that streamlines the use of DAOPHOT-II for photometry, and the PHOTcube extension, which enables efficient and scalable spectral extraction from IFU datacubes.

PHOTfun in particular is a GUI designed to simplify the use of DAOPHOT-II, an example of the main menu is shown in the appendix (see Fig. A.1). The GUI is based on the python package for web apps Shiny (Chang et al. 2025). It works on every set of images and includes the DAOPHOT-II subroutines FIND, PICK, PHOT, PSF, SUBTRACT and DAOMATCH that are necessary for detecting the source, finding their coordinates on every image in the given set, modeling the PSF and finally performing the photometry. This last step is done using the ALLSTAR standalone software included in DAOPHOT-II. While PhotFun itself does not add new capabilities to DAOPHOT-II, it is a user-friendly interface that can be used to perform point-source detection and PSF photometry on any sets of astronomical images, visualizing the most important intermediate results and interactively rejecting model PSF stars as it is shown in Fig. A.2. Interoperability via Simple Application Messaging Protocol (SAMP) to work with software like TOPCAT (Taylor 2005) and DS9 (Smithsonian Astrophysical Observatory 2000) is also enabled.

PHOTcube is an extension integrated into the PHOTfun GUI, allowing users to load the datacube and slice it along the wavelength direction in a set of sequential monochromatic images that can be processed through the PHOTfun GUI by means of standard PSF photometry using DAOPHOT-II. Finally, for each detected source, the PHOTcube extension compiles the monochromatic magnitudes, converts them into fluxes and generates the corresponding spectra.

The full software and source code is available at Github² and PyPi³. To enable the use of DAOPHOT, PHOTfun leverages a Docker⁴ container, which must be installed to ensure compatibility and ease of use across different systems.

3.3. Spectrum extraction: Step by step

The extraction of stellar spectra from the MUSE datacubes using PHOTfun followed these steps: a master target list for each field was generated using the FIND routine. The FoV image corresponding to the white light, which integrates the total flux across all wavelengths, was used for optimal source detection. For PSF modeling, the PICK routine performs an automatic pre-selection of suitable stars; however, it is recommended to manually inspect and refine this selection using the GUI tool, which allows a visual inspection of the light profile of each star (see Fig. A.2). At this stage the master and PSF target lists were defined for each datacube.

The PHOTcube extension slices the datacube and loads it as a sequence of monochromatic images into PHOTfun. Using the defined master and PSF target lists, PSF photometry was performed on each slice with the ALLSTAR routine, measuring the monochromatic fluxes for each target. The individual spectra were then reconstructed by concatenating the measured fluxes across the full wavelength range. This method had been used before by, for example, V18, Olivares Carvajal et al. (2022). The signal-to-noise ratio (SNR) of each spectrum were computed as the mean SNR per wavelength pixel, where the SNR of each pixel were defined as the ratio of flux to its associated uncertainty.

Additionally, using PHOTfun, a color–magnitude diagram (CMD) was produced for each field. This was done by performing PSF photometry on the MUSE pipeline FoV images using

² <https://github.com/ciquezada/photfun>

³ <https://pypi.org/project/photfun/>

⁴ <https://www.docker.com/products/docker-desktop/>

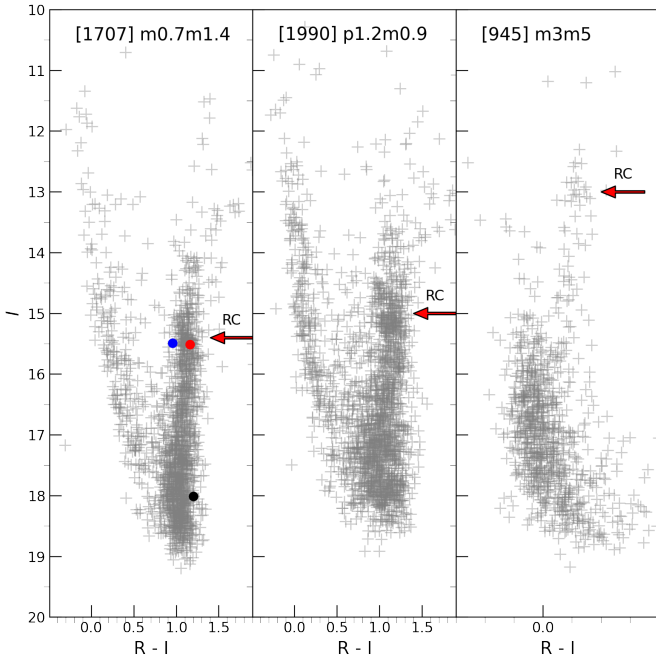


Fig. 2. CMD of three MUSE fields obtained by performing PSF-fitting photometry on the FoV images. The names of the fields and number of detected stars are given inside at the top of each panel. The red arrow marks the position of the RC in each CMD. Also shown in the left panel shows the position of three stars for which we show the extracted spectra in Fig. 3.

the V-Johnson, R-Cousins, and I-Cousins filters, and the same master and PSF target lists. Fig. 2 shows an example of the derived CMD of three fields using the measured instrumental magnitude, two from the MUSE-inner sample and one from the MUSE-outer sample (see Section 3.1). Notable differences in the CMD statistics and photometric depth arise from variations in the field extinction, coverage and integration times across the sample (for instance, Table 1).

The CMDs of the observed fields allowed for partial separation of the bulge population from the foreground disk stars along the line of sight. Specifically, the disk main sequence is clearly visible as a narrow, vertical blue sequence that merges with the bulge population near the main sequence turnoff (MS-TO). For an old stellar population, the MS-TO is typically located approximately 3.2 magnitudes fainter than the red clump (RC) in the I band (Pietrinferni et al. 2004).

Table 2 summarizes the number of stellar spectra extracted for each field, while Fig. 3 presents representative examples from field m0.7m1.4, highlighting the spectral region around the CaT. The selected spectra correspond to stars of varying metallicity, identified based on their position along the red giant branch in the CMD, where redder stars generally indicate higher metallicity. This trend is evident in the middle panel, where the redder star exhibits noticeably stronger CaT absorption features. For comparison, a low SNR spectrum is also shown, illustrating the increased uncertainty in such cases. Nevertheless, all spectra clearly display the CaT absorption lines, which are critical for precise radial velocity and metallicity determinations.

As previously mentioned, another widely used tool for spectral extraction from IFU data is PampelMuse (Kamann et al. 2013), which, in contrast to PHOTfun, requires an external input catalog of sources. Another key distinction between the two

Table 2. Fields characteristics.

Field	N [stars]	μRV_{bc} [km/s]	σ_{RV} [km/s]	RMSE [stars]
MUSE-inner				
p0.2p1.3	1873	-1 ± 6	134 ± 5	11
m0.7m1.4	1707	-21 ± 7	137 ± 7	13
p1.2m0.9	1990	2 ± 6	129 ± 5	13
MUSE-outer				
m5m5	542	-68 ± 8	94 ± 6	6
p1m8	386	-3 ± 9	90 ± 6	4
p3p2	735	30 ± 9	126 ± 7	17
m7m4	577	-78 ± 8	91 ± 6	5
m3m5	945	-43 ± 7	100 ± 5	5
m6p5	605	-78 ± 8	94 ± 6	6
MUSE-V18				
p0m2	1203	9 ± 4	135 ± 3	–
m1p2	861	-8 ± 5	125 ± 3	–
p0p2	496	19 ± 8	137 ± 5	–
p1m1	502	14 ± 7	119 ± 5	–
APOGEE				
m5m2.5	197	-49 ± 14	105 ± 10	8
m5p1.5	132	-66 ± 17	103 ± 12	12
p0m4	348	-0 ± 12	122 ± 9	7
p0p8	304	-8 ± 10	90 ± 7	9
p0p3.5	439	-8 ± 11	120 ± 7	13
p0p2	416	3 ± 13	135 ± 9	10
p5.5p2	490	58 ± 8	99 ± 6	25
p5p4	391	52 ± 10	100 ± 6	16
p5.2m2.2	563	57 ± 8	105 ± 6	30
p4.8m4.4	291	50 ± 11	99 ± 8	7
p1.6m3.6	429	22 ± 10	114 ± 7	14
m2.2m4	330	-36 ± 12	118 ± 9	5
m5m8	200	-53 ± 11	84 ± 8	4
p5p8	189	28 ± 10	73 ± 7	3
GIBS				
p8.4p4.3	209	69 ± 11	86 ± 8	5
p4.3p4.4	208	50 ± 13	98 ± 9	5
m0.7p4.5	210	1 ± 15	112 ± 10	8
m7.7p4.5	210	-70 ± 12	93 ± 9	6
m3.4p4.5	208	-64 ± 13	100 ± 9	7
m0.3m1.4	441	-5 ± 12	135 ± 8	10
m7.5m2.0	210	-86 ± 13	96 ± 9	5
m6.3m2.0	113	-54 ± 19	102 ± 13	14
m4.9m2.0	209	-43 ± 14	108 ± 10	7
m3.5m2.1	111	-58 ± 21	116 ± 15	16
m0.6m2	111	-16 ± 25	137 ± 18	21
p8.4m1.9	209	70 ± 13	95 ± 9	5
p5.2m2.1	112	80 ± 20	111 ± 14	15
p2.4m2.1	318	57 ± 12	115 ± 9	4
p0.3m2.1	435	12 ± 12	135 ± 9	9
p8m3.5	105	76 ± 17	89 ± 12	11
p3.6m3.4	91	52 ± 23	112 ± 16	17
m5.0m3.6	108	-61 ± 19	102 ± 13	14
p1.0m3.9	102	22 ± 22	115 ± 16	16
m6.8m4.7	107	-57 ± 16	84 ± 11	10
p8.5m6.1	209	66 ± 10	77 ± 7	5
p4m6	213	43 ± 12	92 ± 8	4
p0.2m6	454	0 ± 9	98 ± 6	33
m8m6	215	-71 ± 10	80 ± 7	3
m4m6	224	-55 ± 12	93 ± 8	5
p8.3m8.5	193	50 ± 11	79 ± 7	3
p3.9m8.6	207	21 ± 9	68 ± 6	6
m0.4m8.5	415	-8 ± 8	89 ± 6	23
m7.7m8.5	206	-71 ± 11	81 ± 8	4
m3.4m8.6	208	-32 ± 10	79 ± 7	6

Notes. Number of stars adopted in each bulge field, mean RV, σ_{RV} and RMSE. RMSE for New MUSE fields correspond to the double Gaussian fitting. V18 RMSE are missing because they are not reported in the original paper.

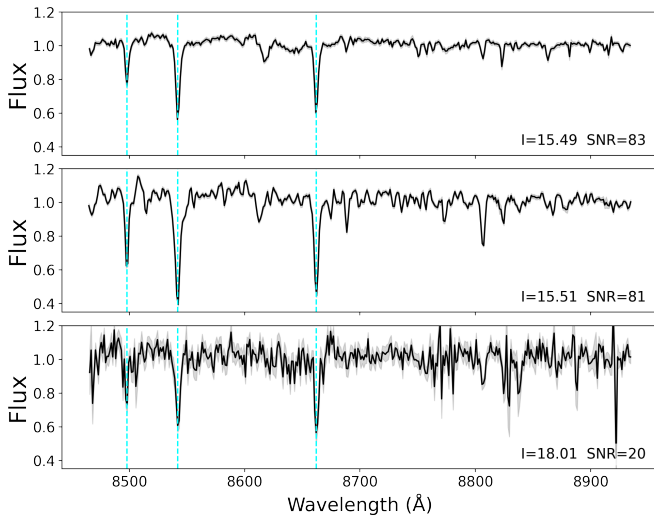


Fig. 3. CaT region of the normalized spectra (Sect. 3.3) for three stars within the field m0.7m1.4. Vertical cyan lines mark the position of the three CaT lines. The top and middle panels show the two stars marked as blue (top) and red (bottom) dots in the CMD shown in the left panel of Fig. 2. Their position in the CMD and the strength of their CaT lines suggest that they are metal-poor and a metal-rich star, respectively. The bottom panel shows the faint star marked as a black dot in the left panel of Fig. 2. A gray shaded area shows the flux error in the three panels, as estimated from the magnitude errors provided by DAOPHOT. Due to the different SNR of the three spectra (shown in the figure labels), the gray shaded area is only visible in the bottom panel.

methods lies in the approach to sky subtraction. While PampelMuse relies on the global sky subtraction provided by the MUSE pipeline, PHOTfun – via DAOPHOT-II – computes a local sky estimate within an annulus around each detected source. This localized sky subtraction approach allowed our method to effectively mitigate residual sky features that were not fully corrected by the standard pipeline. Furthermore, science fields exhibiting significant sky variability – such as star-forming regions – greatly benefit from the ability to measure and subtract the local sky background. Finally, DAOPHOT-II is optimized to perform PSF photometry in crowded fields, thus mitigating the problem of blending. Visual inspection also helped discarding blends, as two stars with different RVs show broader or double CaT lines in their spectra.

Figure 4 illustrates a comparison between spectra extracted using PHOTfun–PHOTcube (black line) and PampelMuse (red line) for a bright star (top panel), a faint star (middle panel), and an empty sky region (bottom panel). The bottom panel reveals residuals from imperfect sky subtraction around strong OH emission lines, highlighted by vertical cyan lines. These residuals were also present in the PampelMuse spectra, particularly around the OH features, whereas the spectra extracted with PHOTfun are notably smoother in these regions, demonstrating the improved sky handling of our method.

3.4. Radial velocities

Individual star RVs along the line of sight were determined by measuring the Doppler shift of the spectra in the CaT wavelength range, from 8465 Å to 8935 Å. Each spectrum was cropped to this region and the continuum were normalized by fitting a fourth-degree polynomial. The observed spectrum

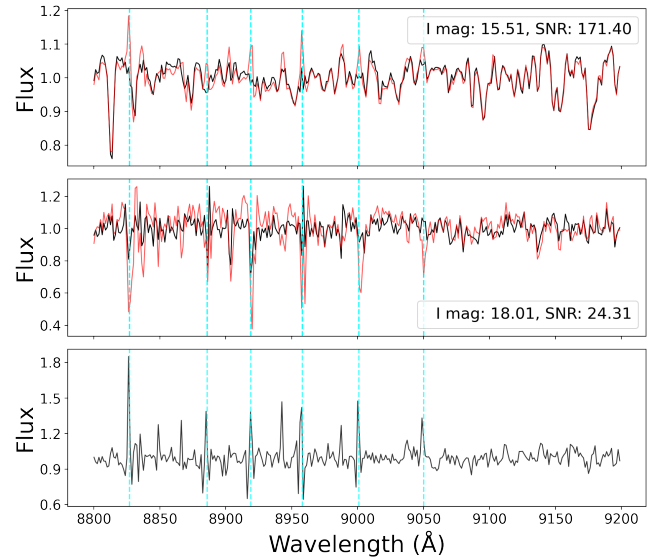


Fig. 4. Comparison with PampelMuse. The top and middle panels show the normalized spectra (Sect. 3.3) of a bright and a faint star respectively, as extracted by PHOTfun in black, and red by PampelMuse. Both stars belong to the field m0.7m1.4. Vertical dashed cyan lines show the position of strong OH sky lines. The bottom panel shows the spectrum of a region of the image devoid of stars. Because the MUSE pipeline performs the subtraction of a single master sky spectrum, what we are seeing in the bottom panel shows the residual of this subtraction. These residuals are larger around the strong OH sky lines, consequently also the PampelMuse-extracted spectra show non-negligible residuals.

was then cross-correlated with a small grid corresponding to a subset of synthetic templates generated using TurboSpectrum (Alvarez & Plez 1998), together with MARCS model atmospheres (Gustafsson et al. 2008) and the Gaia-ESO Survey line list published in Heiter et al. (2021), this subset is not complete –it corresponds to a sparse grid– and it was just intended to obtain RV, nevertheless, covering the surface parameter range $T_{\text{eff}}=4000\text{--}6000$ K, $\log g=1.5\text{--}4.5$ dex and $[M/H]=-1$ to $+1$ dex. First, a cross-correlation was performed to obtain an initial guess of the RV using a synthetic spectrum randomly selected from the grid. The spectrum was then rest-frame corrected for the resulting RV guess, and a χ^2 test was then done to find the best fitting synthetic spectrum for that particular star over the entire subset of synthetic spectra. A second iteration to find the final RV was then performed cross-correlating the observed spectrum with the synthetic one. No interpolation was done, as for RV measurements a perfect match between the observed and template spectra was not necessary. This step yielded the final value for the RV, together with the rest-frame corrected spectrum for each star.

We visually inspected the selected template for each star and the corresponding cross-correlation function (CCF) to discard spurious results, typically excluding 10–30% of the faintest stars from each field. The uncertainty in the RV was calculated using one of the two formulas presented in Valenti et al. (2018) based on simulated MUSE spectra and calibrated for their observed data for different SNR and metallicity. For this work, given the metallicity distribution of the bulge, we used the RV uncertainty of a solar-metallicity dwarf star (0.0 dex) which was the most representative case. This was given by

$$\ln(\epsilon_{RV}) = 4.624 - 1.023 \ln(S/N) - 0.159[Fe/H] + 0.120[Fe/H]^2. \quad (1)$$

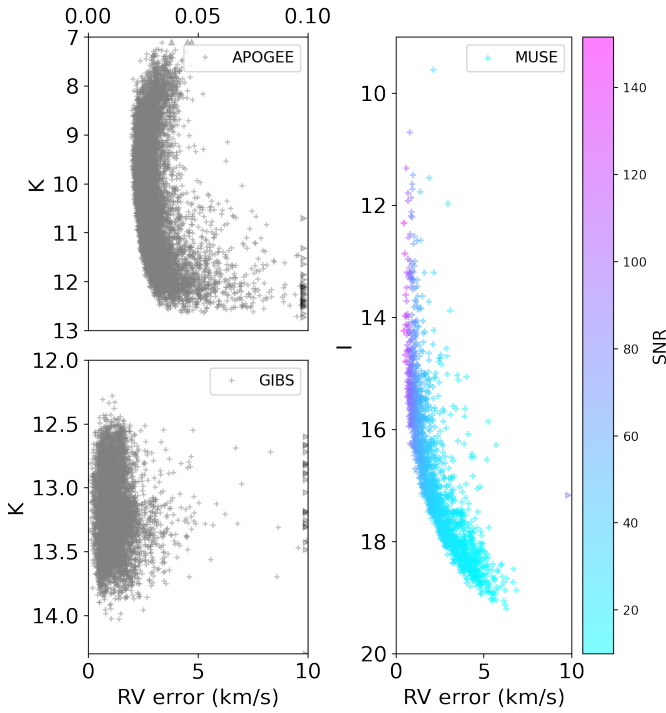


Fig. 5. RV error versus magnitude for the APOGEE, GIBS, and MUSE samples. The MUSE example shown in the right-hand plot corresponds to the field m0.7m1.4 (see Fig. 2). MUSE errors are estimated from the Equation (1). Symbols show individual stars; arrows indicate values beyond axis limits. Note the differing axis scales: APOGEE RV errors are significantly smaller.

An example of the derived uncertainty in RV is shown in Fig. 5. The derived RVs are already in the heliocentric reference frame, as this correction is performed by the MUSE pipeline. In order to transform them to a galactocentric reference frame, we use the formula Zoccali et al. (for example, 2014),

$$V_{GC} = V_{HC} + 220 \sin(l) \cos(b) + 16.5 [\sin(b) \sin(25) + \cos(b) \cos(25) \cos(l - 53)]. \quad (2)$$

In order to derive the RV distribution of bonafide bulge stars in each field, we used the approach illustrated in Fig. 6. Each MUSE field samples a combination of bulge plus disk foreground stars. Based on the CMD, we isolated bonafide disk stars in the bright blue sequence highlighted in cyan in Fig. 6 (left). The top right panel of the same figure confirms that indeed, these stars were characterized by narrower RV distribution, compared to the total sample. The mean and the dispersion of this distribution were derived by a Gaussian fitting (bottom-right), and it was assumed that they represent the intrinsic RV and σ_{RV} of the disk in this field. The RV and σ_{RV} of the bulge was then derived by fitting the total observed distribution as the sum of two Gaussian profiles; the disk with the fixed parameters above, and the bulge with free parameters to be constrained. The latter fit was performed by means of the PyMC package (Salvatier et al. 2016) which runs a Markov Chain Monte Carlo (MCMC) search for the best-fitting parameters. The best-fitting Gaussian profiles for the field m0.7m1.4 are shown in Fig. 7, where the red profile corresponds to the bulge which has mean RV = -21 km/s and $\sigma_{RV} = 137$ km/s, and the cyan one to the disk which has

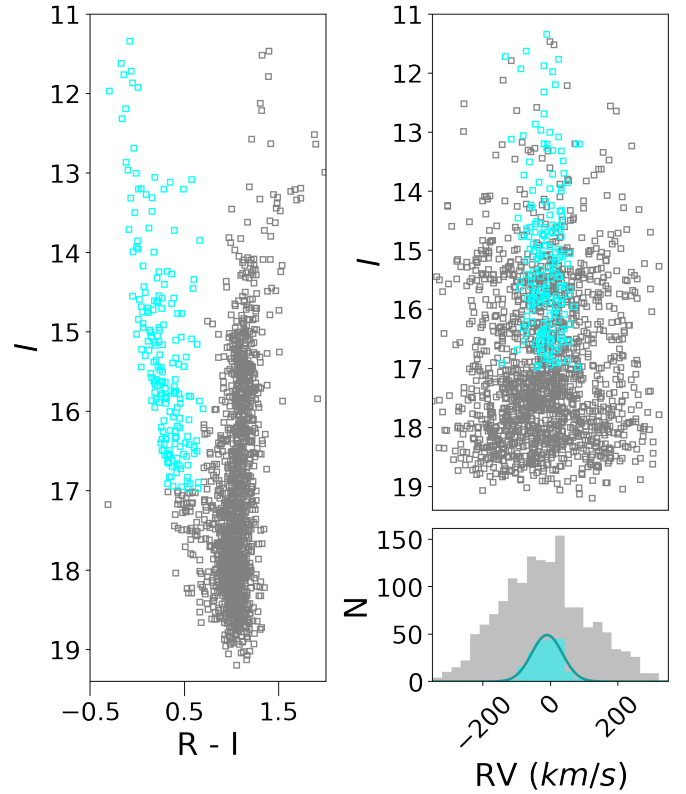


Fig. 6. The left panel shows the CMD of the field m0.7m1.4. In cyan, we have highlighted the disk subsample chosen to be a representation of the whole disk sample (in this field we chose to cut a magnitude $I < 17$ and a color $R - I < 0.8$). Top right panel shows the I magnitude vs the RV also with the whole disk sample highlighted. The bottom right panel shows the histogram with the highlighted sample of the disk.

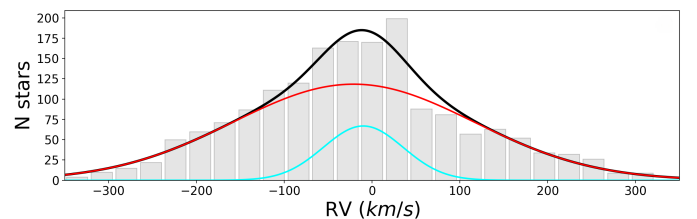


Fig. 7. Fit of the two component Gaussian profiles in the m0.7m1.4 field. The black line show the best fit that is a sum of the cyan profile that correspond to the disk distribution and the red profile that correspond to the bulge.

a mean RV = -10 km/s and $\sigma_{RV} = 45$ km/s. The disk RV values are comparable to the kinematic maps in Ness et al. (2016), Fig. 7.

Concerning the literature data, we used the V18 RV and σ_{RV} as they are provided in the paper. In contrast, for the GIBS and APOGEE data, where in each field we fitted a single Gaussian profile to the whole distribution of individual stars galactocentric RV measurements provided in the catalogs, as they were already cleaned out of foreground contamination. Indeed, GIBS selected targets were in a narrow magnitude range centered in the bulge RC, where disk contamination is negligible. For APOGEE data, the selection of stars within 3.5 kpc from the galactic center already minimized foreground contamination. The RVs and σ_{RV} for all the fields; the new MUSE data and the literature ones,

Table 3. Coefficients of the kinematic maps for the RV and σ_{RV} .

RV							
	A	B	C	D	E	F	
Value	-1.96	-0.10	0.08	81.05	-0.95	0.19	
Error	3.99	0.10	0.10	18.81	0.80	0.08	
σ_{RV}							
	A	B	C	D	E	r	s
Value	45.54	53.36	281.61	-0.12	36.30	693.96	21.60
Error	11.96	13.68	38.47	0.06	4.87	169.46	6.41

Notes. Derived from analytical equations described in Z14. The resulting best-fitting coefficients are listed along with their uncertainties.

are listed in Table 2. We also report the root mean squared error (RMSE) of each individual and double Gaussian fit in Table 2. The RMSE values for the V18 fields are omitted since they were not reported in the original article. To avoid the low statistic in the fitting, for fields with fewer than 150 stars we calculated the arithmetic mean RV and the associated σ_{RV} with the traditional formula. We obtained the same result as the Gaussian fitting with less than 1% of difference; hence, we kept the values of the fitting for consistency.

4. Kinematic maps

The kinematic maps are updated by fitting phenomenological analytical equations previously used in Z14 to model the bulge RV and σ_{RV} , defined as follows:

$$RV_{GC} = (A + Bb^2) + (Cb^2)l + (D + Eb^2)\tanh(Fl), \quad (3)$$

$$\sigma_{RV_{GC}} = (A + Be^{-b^2/C}) + Dl^2 + (Ee^{-b^4/r})e^{-l^2/s}. \quad (4)$$

The fitting process is performed using MCMC methods, following the same procedure as in the previous step, to derive the best-fitting coefficients. The resulting coefficients are presented in Table 3, and the associated corner plots are shown in Figs. B.1 and B.2 in the appendix.

The final kinematic map of RV, with contours displayed in steps of 10 km/s and the corresponding map of the σ_{RV} , including its contours, is shown in Fig. 8. Both figures also display the residuals of the fit along Galactic latitude and longitude. It is worth saying that the residuals do not exceed 10% of the model value, remaining within the error bars. Compared with previous kinematic maps in Z14, the updated map of RV exhibits only minor differences, particularly at the top edge where more constraints were added. The difference was within the expected uncertainties and does not significantly alter the overall cylindrical rotation trend. The map of the σ_{RV} shows slightly more differences, especially near the Galactic plane. The updated map is better constrained in this region, the absence of the “wing-like” shape along the Galactic plane compared to the previous version in Z14 (see contours in Fig. 1) is attributed to the additional measurements, altering the global shape to a visually boxier/regular morphology. The updated map still shows a central σ_{RV} peak elongated along the galactic latitude but smoother than before. A more detailed visual difference with comparison maps could be found in Figs. C.1 and C.2 in the appendix.

We also evaluated the inclusion of external catalogs such as BRAVA and ARGOS, which cover regions similar to the outer areas of our survey. The comparison revealed differences of

± 15 km/s in the mean RV and ± 10 km/s in σ_{RV} , with a systematic offset of approximately 4 km/s in σ_{RV} . These discrepancies fall within the expected uncertainties, indicating general consistency with our velocity map. We decided not to include them in the present model, given our primary goal of improving constraints in the inner regions, which were poorly sampled by these surveys.

5. Discussion

From our results, the updated mean RV map confirms the cylindrical rotation of the bulge reinforced by more the latitude coverage of the new observations. This result agrees well with bulge spectroscopic surveys such as BRAVA (Kunder et al. 2012), ARGOS (Freeman et al. 2013) and Gaia ESO survey (Rojas-Arriagada et al. 2014) where the bulge was consistently found to rotate cylindrically.

The updated σ_{RV} map also changed with the new constraints. The σ_{RV} peak is now smoother than in the previous version, but it is still vertically extended. Near the plane, it no longer shows the wings that were observed in the σ_{RV} map by Z14. Comparisons of the maps by Z14 against models have been made in Gonzalez et al. (2016). In that case, the model was a pure disk galaxy, simulated by means of an N-body code based on Cole et al. (2014). Both the Z14 and the present σ_{RV} map agree with that model. The latter shows a vertically extended peak caused by the elongated orbits of stars in the bar and boxy-peanut. The shape of the peak depend on the angle between the line of sight and the bar major axis (in this case 20°). That comparison confirms that the mere presence of a bar, with its orbit anisotropy, can produce a peak in the projected σ_{RV} . However, this finding is not sufficient to explain the peak observed in the data, as the latter could also be produced by a larger contraction of mass in the innermost region. The model presented in Gonzalez et al. (2016) does not show the -wings- close to the plane that were present in the map by Z14 and have disappeared now, thanks to the additional observational data.

A more recent work from Khoperskov et al. (2025) shows RV maps of the MW bulge using an orbit superposition method. The data were taken from APOGEE DR17, and used to calculate and rewind the stellar orbits, assuming the same fixed gravitational potentials as in Sormani et al. (2022) and first released in Portail et al. (2017). Different orbit snapshots were superposed in order to reconstruct the RV kinematics maps, specifically the σ_{RV} map is shown in the Fig. 6 in Khoperskov et al. (2025). The σ_{RV} map was consistent with the central peak vertically elongated, and no excess of σ_{RV} was shown in the plane as in the present work.

The works mentioned above were based on models of pure disk galaxies, and reproduce well the observed kinematics of the bulge. Nonetheless, the presence of a spheroidal component in the bulge is clearly demonstrated by several independent observations (for example, Zoccali et al. 2017; Lim et al. 2021, and references therein). In order to understand the origin of σ_{RV} peak, we are currently comparing the present data with the CIELO (Tissera et al. 2025) suite of cosmological simulation (Acosta-Tripailao et al., in preparation).

In closing, we note that the present data do not allow us to impose constraints on the kinematics of the nuclear stellar disk. Indeed, according to the model of Sormani et al. (2022), in the MW the NSD would be very small, as shown by the white contour in the central region of Fig. 8. The present data are too sparse, in that region, to include the effect of a NSD. In the

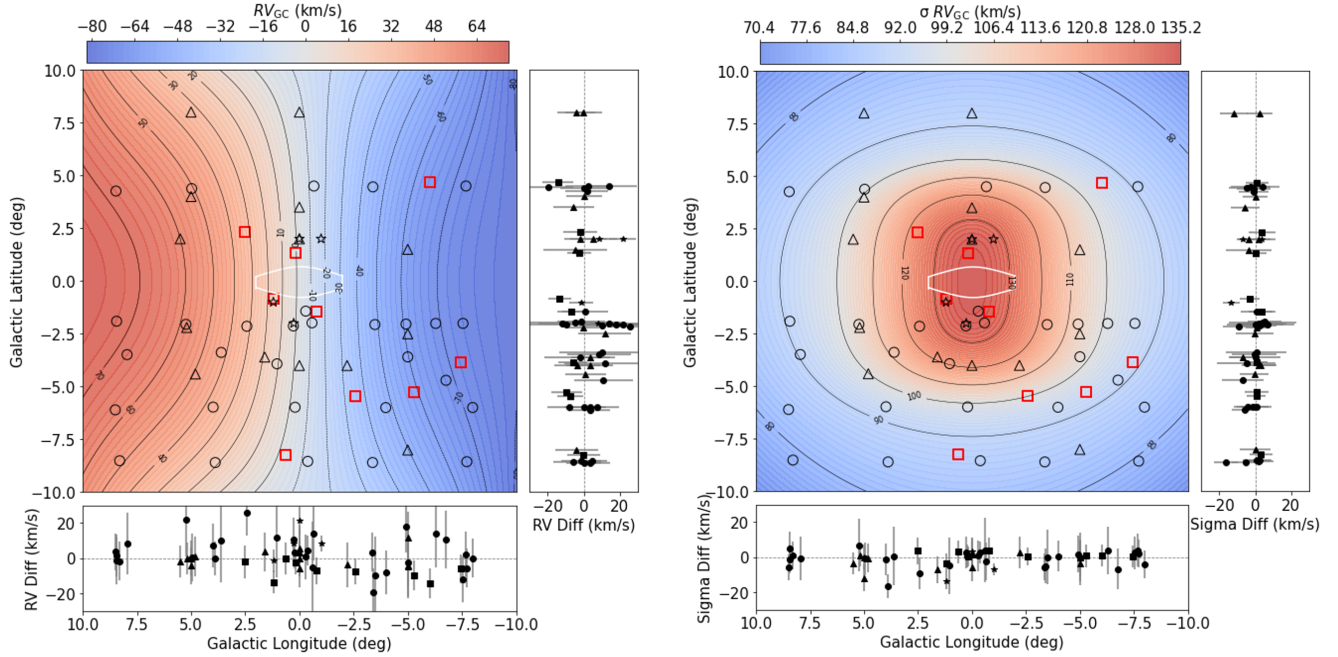


Fig. 8. Updated maps of the bulge RV; colors and black contours show the RV profile fitted by the MCMC in steps of 10 km/s. The different marks are showing the different source of the measurement following the same description as in Fig. 1. The fiducial NSD iso-contour from Sormani et al. (2022) is shown as the white line representing where the NSD has a density of $6 \times 10^7 M_{\odot}/\text{deg}^2$. Left panel correspond to the new mean RV map, in comparison with the previous map, the differences are not stunning but expected. Right panel shows the map of the σ_{RV} , comparing with the previous map, the differences are clear near the galactic plane where new constraints were added. See figures in Appendix C for a more detailed comparison.

future, it would be especially interesting to fill this region, in order to provide more stringent constraints about the presence (or absence) of a clear kinematic signature of the presence of a NSD (for example, see discussion in Zoccali et al. 2024).

6. Summary and conclusions

In this study, we presented an update to the known kinematic maps of the MW bulge, incorporating 28 new measurements of RV and σ_{RV} in the line of sight based on MUSE and APOGEE data. These measurements complement previous studies, such as the GIBS survey and V18, by adding spatial coverage closer to the Galactic plane. The updated maps provide new insights into the kinematics of the bulge. Specifically, we observe that the σ_{RV} contours exhibit a boxier morphology compared to previous results, with a significant reduction in the “wing-like” extensions along the Galactic plane. The previous σ_{RV} central peak studied in V18 is still visible, however it is smoother. While the former was more elongated along the latitude, likely because now the contours near the plane are better constrained.

These new findings can be further complemented by studying the separated kinematics of the different stellar components in the bulge. Measuring the chemical abundances of the same stars included in the present sample would allow a separation into metal-rich and metal-poor components, whose corresponding RV in previous works have been shown to be different in the inner bulge. The RV indicates a faster rotation for the metal-rich population and a slower rotation for the metal-poor one (Ness et al. 2013; Rojas-Arriagada et al. 2020; Olivares Carvajal et al. 2024). Interestingly, the σ_{RV} near the plane is higher for the metal-rich component than for the metal-poor one, as recently shown by Bojin et al. (2024). This result appears counterintuitive, since the metal-rich population is thought to trace the bar

structure, where a more coherent rotation – and thus a lower σ_{RV} – would be expected compared to the metal-poor component. Studying the σ_{RV} in this context can provide important insights. A higher σ_{RV} in the metal-rich population may indicate a higher stellar mass density (Rix et al. 2024; Horta Darrington et al. 2025), or reflect the anisotropy of the stellar orbits in the bar, the high σ_{RV} could be tracing the vertex deviation (Babusiaux et al. 2010; Babusiaux 2016; Simion et al. 2021). Furthermore, the differences in σ_{RV} constraints formation scenarios consequences like the kinematic fractionation (Debattista et al. 2017; Fragkoudi et al. 2018), predicted in the disk secular evolution model, which explains that the differences in the current spatial distribution of the stellar populations depend on the different initial kinematics of these components.

As part of this work, we released a new Python-based photometry package PHOTfun, which integrates DAOPHOT-II into a GUI to easily perform robust PSF photometry of any set of science images, and the extension PHOTcube that extends the capability of the software to work on any IFU datacube in order to extract sources spectrum via PSF photometry. This tool enables efficient and robust extraction of spectra from high-density regions, ensuring reliable measurements. By reanalyzing previously published datasets, we also emphasized the value of using updated techniques to achieve consistent results.

Acknowledgements. This work is funded by ANID, Millenium Science Initiative, ICN12_009 awarded to the Millennium Institute of Astrophysics (M.A.S.), by the ANID BASAL Center for Astrophysics and Associated Technologies (CATA) through grant FB210003, and by FONDECYT Regular grant No. 1230731. C. Q. Z. acknowledges support from the National Agency for Research and Development (ANID), Scholarship Program Doctorado Nacional 2021 – 21211884, ANID, ESO SSDF 13/23 D grant. A.R.A. acknowledges support from DICYT through grant 062319RA. E.V. acknowledges the Excellence Cluster ORIGINS Funded by the Deutsche Forschungsgemeinschaft (DFG, German Research Foundation) under Germany’s Excellence Strategy – EXC-2094-390783311.

A.M. acknowledges support from the project “LEGO – Reconstructing the building blocks of the Galaxy by chemical tagging” (PI A. Mucciarelli), granted by the Italian MUR through contract PRIN 2022LLP8TK_001. A.V.N. acknowledges support from the National Agency for Research and Development (ANID), Scholarship Program Doctorado Nacional 2020 – 21201226, ANID.

References

- Abdurro’uf, Accetta, K., Aerts, C., et al. 2022, *ApJS*, 259, 35
- Alvarez, R., & Plez, B. 1998, *A&A*, 330, 1109
- Arsenault, R., Madec, P. Y., Hubin, N., et al. 2008, *SPIE Conf. Ser.*, 7015, 701524
- Athanassoula, E. 2005, *MNRAS*, 358, 1477
- Babusiaux, C. 2016, *PASA*, 33, e026
- Babusiaux, C., Gómez, A., Hill, V., et al. 2010, *A&A*, 519, A77
- Bacon, R., Accardo, M., Adjali, L., et al. 2010, *SPIE Conf. Ser.*, 7735, 773508
- Bensby, T., Feltzing, S., Gould, A., et al. 2017, *A&A*, 605, A89
- Boin, T., Di Matteo, P., Khoperskov, S., et al. 2024, *A&A*, 692, A13
- Bournaud, F., Elmegreen, B. G., & Martig, M. 2009, *ApJ*, 707, L1
- Carollo, C. M., Scarlata, C., Stiavelli, M., Wyse, R. F. G., & Mayer, L. 2007, *ApJ*, 658, 960
- Chang, W., Cheng, J., Allaire, J., et al. 2025, *shiny: Web Application Framework for R*, R package version 1.10.0.9000
- Clarkson, W. I., Sahu, K. C., Anderson, J., et al. 2011, *ApJ*, 735, 37
- Cole, D. R., Debattista, V. P., Erwin, P., Earp, S. W. F., & Roškar, R. 2014, *MNRAS*, 445, 3352
- Debattista, V. P., Ness, M., Gonzalez, O. A., et al. 2017, *MNRAS*, 469, 1587
- Debattista, V. P., Gonzalez, O. A., Sanderson, R. E., et al. 2019, *MNRAS*, 485, 5073
- Dekel, A., & Burkert, A. 2014, *MNRAS*, 438, 1870
- Elmegreen, B. G., Bournaud, F., & Elmegreen, D. M. 2008, *ApJ*, 688, 67
- Fragkoudi, F., Di Matteo, P., Haywood, M., et al. 2018, *A&A*, 616, A180
- Freeman, K., Ness, M., Wylie-de-Boer, E., et al. 2013, *MNRAS*, 428, 3660
- Garrison-Kimmel, S., Hopkins, P. F., Wetzel, A., et al. 2018, *MNRAS*, 481, 4133
- Genzel, R., Burkert, A., Bouché, N., et al. 2008, *ApJ*, 687, 59
- Genzel, R., Jolly, J. B., Liu, D., et al. 2023, *ApJ*, 957, 48
- Gonzalez, O. A., Gadotti, D. A., Debattista, V. P., et al. 2016, *A&A*, 591, A7
- Gran, F., Zoccali, M., Contreras Ramos, R., et al. 2019, *A&A*, 628, A45
- Gustafsson, B., Edvardsson, B., Eriksson, K., et al. 2008, *A&A*, 486, 951
- Heiter, U., Lind, K., Bergemann, M., et al. 2021, *A&A*, 645, A106
- Hopkins, P. F., Bundy, K., Croton, D., et al. 2010, *ApJ*, 715, 202
- Horta Darrington, D., Petersen, M. S., & Peñarrubia, J. 2025, *MNRAS*, 538, 998
- Howard, C. D., Rich, R. M., Clarkson, W., et al. 2009, *ApJ*, 702, L153
- Immeli, A., Samland, M., Gerhard, O., & Westera, P. 2004, *A&A*, 413, 547
- Kamann, S., Wisotzki, L., & Roth, M. M. 2013, *A&A*, 549, A71
- Kauffmann, G., White, S. D. M., & Guiderdoni, B. 1993, *MNRAS*, 264, 201
- Khoperskov, S., Di Matteo, P., Steinmetz, M., et al. 2025, *A&A*, 700, A90
- Kunder, A., Koch, A., Rich, R. M., et al. 2012, *AJ*, 143, 57
- Lim, D., Koch-Hansen, A. J., Chung, C., et al. 2021, *A&A*, 647, A34
- Majewski, S. R., Schiavon, R. P., Frinchaboy, P. M., et al. 2017, *AJ*, 154, 94
- Molaeinezhad, A., Falcón-Barroso, J., Martínez-Valpuesta, I., et al. 2016, *MNRAS*, 456, 692
- Ness, M., Freeman, K., Athanassoula, E., et al. 2013, *MNRAS*, 432, 2092
- Ness, M., Zasowski, G., Johnson, J. A., et al. 2016, *ApJ*, 819, 2
- Neumayer, N., Seth, A., & Böker, T. 2020, *A&A Rev.*, 28, 4
- Olivares Carvajal, J., Zoccali, M., Rojas-Arriagada, A., et al. 2022, *MNRAS*, 513, 3993
- Olivares Carvajal, J., Zoccali, M., De Leo, M., et al. 2024, *A&A*, 687, A312
- Pasquini, L., Avila, G., Allaert, E., et al. 2000, *SPIE Conf. Ser.*, 4008, 129
- Patsis, P. A., Skokos, C., & Athanassoula, E. 2002, *MNRAS*, 337, 578
- Pietrinferni, A., Cassisi, S., Salaris, M., & Castelli, F. 2004, *ApJ*, 612, 168
- Portail, M., Wegg, C., Gerhard, O., & Martínez-Valpuesta, I. 2015, *MNRAS*, 448, 713
- Portail, M., Gerhard, O., Wegg, C., & Ness, M. 2017, *MNRAS*, 465, 1621
- Queiroz, A. B. A., Anders, F., Chiappini, C., et al. 2020, *A&A*, 638, A76
- Renzini, A., Gennaro, M., Zoccali, M., et al. 2018, *ApJ*, 863, 16
- Rich, R. M., Reitzel, D. B., Howard, C. D., & Zhao, H. 2007, *ApJ*, 658, L29
- Rix, H.-W., Chandra, V., Zasowski, G., et al. 2024, *ApJ*, 975, 293
- Rojas-Arriagada, A., Recio-Blanco, A., Hill, V., et al. 2014, *A&A*, 569, A103
- Rojas-Arriagada, A., Zasowski, G., Schultheis, M., et al. 2020, *MNRAS*, 499, 1037
- Salvatier, J., Wiecki, T. V., & Fonnesbeck, C. 2016, PyMC3: Python probabilistic programming framework, Astrophysics Source Code Library [[record ascl:1610.016](#)]
- Shen, J., Rich, R. M., Kormendy, J., et al. 2010, *ApJ*, 720, L72
- Simion, I. T., Belokurov, V., Irwin, M., et al. 2017, *MNRAS*, 471, 4323
- Simion, I. T., Shen, J., Kposov, S. E., et al. 2021, *MNRAS*, 502, 1740
- Smithsonian Astrophysical Observatory 2000, SAOImage DS9: A utility for displaying astronomical images in the X11 window environment, Astrophysics Source Code Library [[record ascl:0003.002](#)]
- Sormani, M. C., Sanders, J. L., Fritz, T. K., et al. 2022, *MNRAS*, 512, 1857
- Stetson, P. B. 1987, *PASP*, 99, 191
- Ströbele, S., La Penna, P., Arsenault, R., et al. 2012, *SPIE Conf. Ser.*, 8447, 844737
- Surot, F., Valenti, E., Gonzalez, O. A., et al. 2020, *A&A*, 644, A140
- Tacchella, S., Dekel, A., Carollo, C. M., et al. 2016, *MNRAS*, 458, 242
- Tadaki, K.-i., Genzel, R., Kodama, T., et al. 2017, *ApJ*, 834, 135
- Taylor, M. B. 2005, in *Astronomical Society of the Pacific Conference Series*, 347, *Astronomical Data Analysis Software and Systems XIV*, eds. P. Shopbell, M. Britton, & R. Ebert, 29
- Tissera, P. B., Bignone, L., Gonzalez-Jara, J., et al. 2025, *A&A*, 697, A134
- Tumlinson, J. 2010, *ApJ*, 708, 1398
- Valenti, E., Zoccali, M., Gonzalez, O. A., et al. 2016, *A&A*, 587, L6
- Valenti, E., Zoccali, M., Mucciarelli, A., et al. 2018, *A&A*, 616, A83
- Weilbacher, P. M., Palsa, R., Streicher, O., et al. 2020, *A&A*, 641, A28
- Zoccali, M., & Valenti, E. 2024, arXiv e-prints [arXiv:2412.01607]
- Zoccali, M., Gonzalez, O. A., Vasquez, S., et al. 2014, *A&A*, 562, A66
- Zoccali, M., Vasquez, S., Gonzalez, O. A., et al. 2017, *A&A*, 599, A12
- Zoccali, M., Rojas-Arriagada, A., Valenti, E., et al. 2024, *A&A*, 684, A214

Appendix A: PHOTfun GUI preview.

PHOTfun offers a GUI that streamlines the use of DAOPHOT-II for PSF photometry. As shown in Fig. A.1, the interface organizes all core functions into interactive tabs, allowing users to load FITS images, detect sources, model the PSF, and execute photometric analysis using standard DAOPHOT-II routines such as FIND, PHOT, PSF etc. Parameters are adjustable directly within the GUI, and key intermediate results are visualized in real time, thus reducing the reliance on command-line input and making the workflow more accessible and efficient.

An additional component of PHOTfun is the interactive PSF star selection (Fig. A.2), which displays image cutouts and light profiles for each candidate PSF star. This feature helps users identify and exclude stars with blended or asymmetric profiles. The GUI also supports SAMP-based communication with external tools like TOPCAT and DS9. Additionally, the integrated PHOTcube module extends these capabilities to IFU datacubes, enabling spectra extraction from monochromatic image slices using the same PSF photometric framework.

The screenshot displays the PHOTfun GUI with the following components:

- Loaded Data Panel:** A table listing loaded FITS files.

FITS	File
0	12_white.fits
5	fsr_1469_01_c1.fits
18	fsr_1482_02_c1.fits
29	fsr_1469_01_c1_als_sub.fits
36	fsr_1482_02_c1_als_sub.fits

 Below the table, it indicates 'Viewing rows 1 through 5 of 9' and includes a 'Delete Selected' button.
- Navigation Tabs:** Files, DAOPhot (selected), Target Selection, Export, PHOTcube, Logs.
- FITS Preview:** A central image showing a star field with red circles marking selected targets. The axes range from 0 to 2000 pixels.
- Control Panel:**
 - Tabs: FIND, PHOT, PICK, PSF, SUBTRACT.
 - Selected routines: ALLSTAR, DAOMATCH, MASTER, Settings.
 - Select FITS: [5] fsr_1469_01_c1.fits
 - Select PSF model: [26] fsr_1469_01_c1.psf
 - Select Targets: [21] fsr_1469_01_c1.ap
 - ALLSTAR button.
 - Fitting Radius (px): 2.5
 - Inner Sky (px): 12
 - Outer Sky (px): 20
 - Recenter button (checked).

Fig. A.1. PHOTfun graphical user interface. On the left panel, the loaded files are displayed. At the top center, a set of tabs provides access to the available actions, including the PHOTcube extension. The central bottom panel shows a preview of the selected FITS image, with red circles marking the selected targets. On the right panel, the user can access the available DAOPHOT-II and ALLSTAR routines along with their configurable parameters.

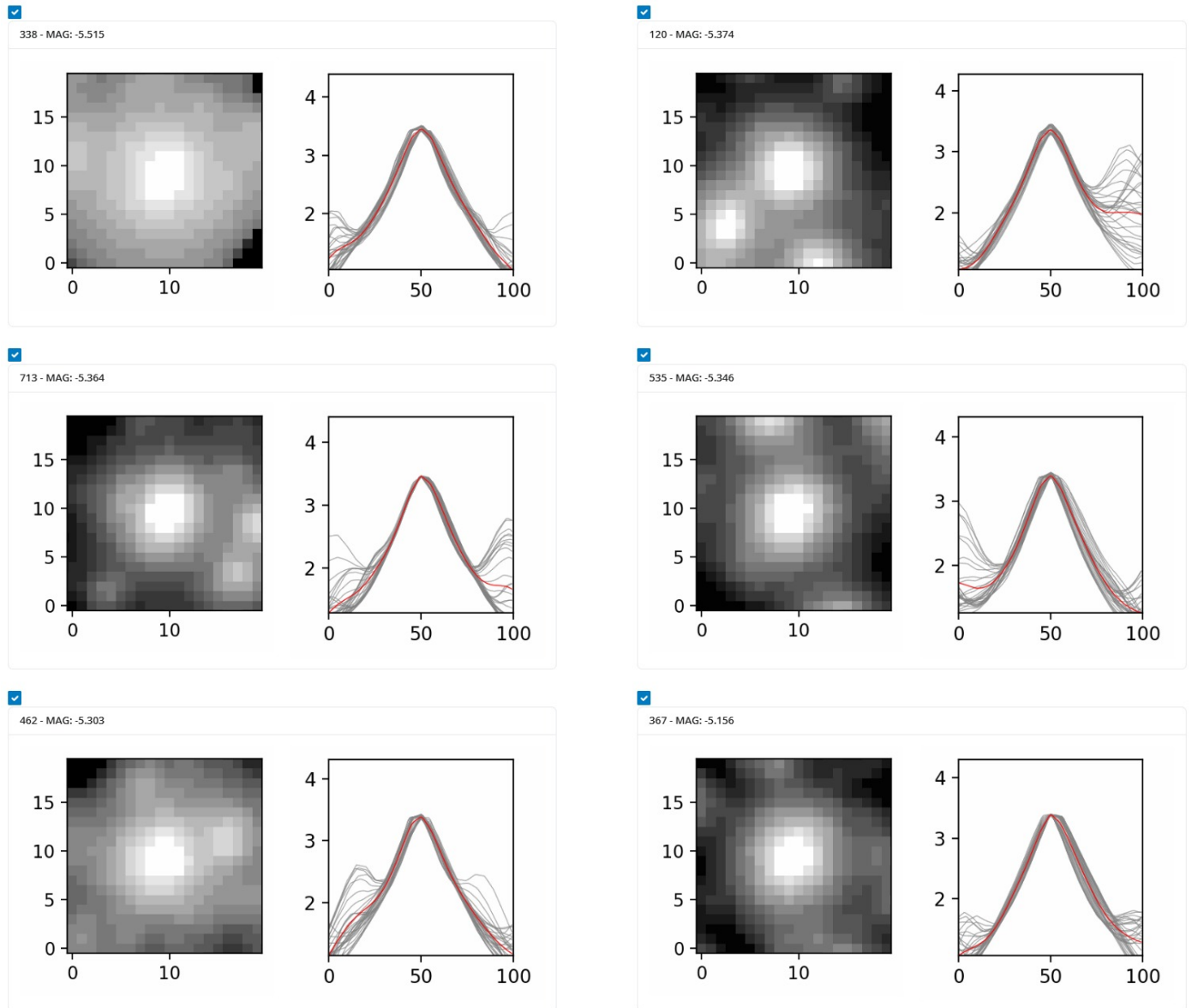


Fig. A.2. Example of the PSF star selection panel provided by the software. For each candidate star, the interface displays its 20x20 pixels image alongside its light profile, also in 20 pixels (even if the PSF fitting radius is fewer than 10 pixels). Each line in the profile represents a line crossing through the star center, with consecutive lines corresponding to rotated profiles at different angles. The solid line indicates the averaged profile, which ideally approximates a Gaussian shape. Ideally one rejects the profiles which have contamination of near sources in the inner user selected fitting radius.

Appendix B: Corner plots for the kinematic maps fitting.

To evaluate the robustness of the kinematic model fits, we examined the full posterior distribution of the parameters governing the analytic expressions for the mean radial velocity and velocity dispersion maps. The resulting corner plots from the MCMC sampling are shown in Figures B.1 and B.2. These plots display the parameters distribution along with their covariances,

providing a diagnostic tool for identifying degeneracies or parameters that are poorly constrained.

For both the RV and σ_{RV} models, the posteriors distribution exhibits well defined Gaussian profiles, indicating that the inferred parameters and their uncertainties are robust. This confirms efficient convergence of the MCMC chains, and validates the statistical reliability of the fitted kinematic profiles. The resulting coefficients, listed in Table 3, are thus representative of a stable solution well constrained by the data.

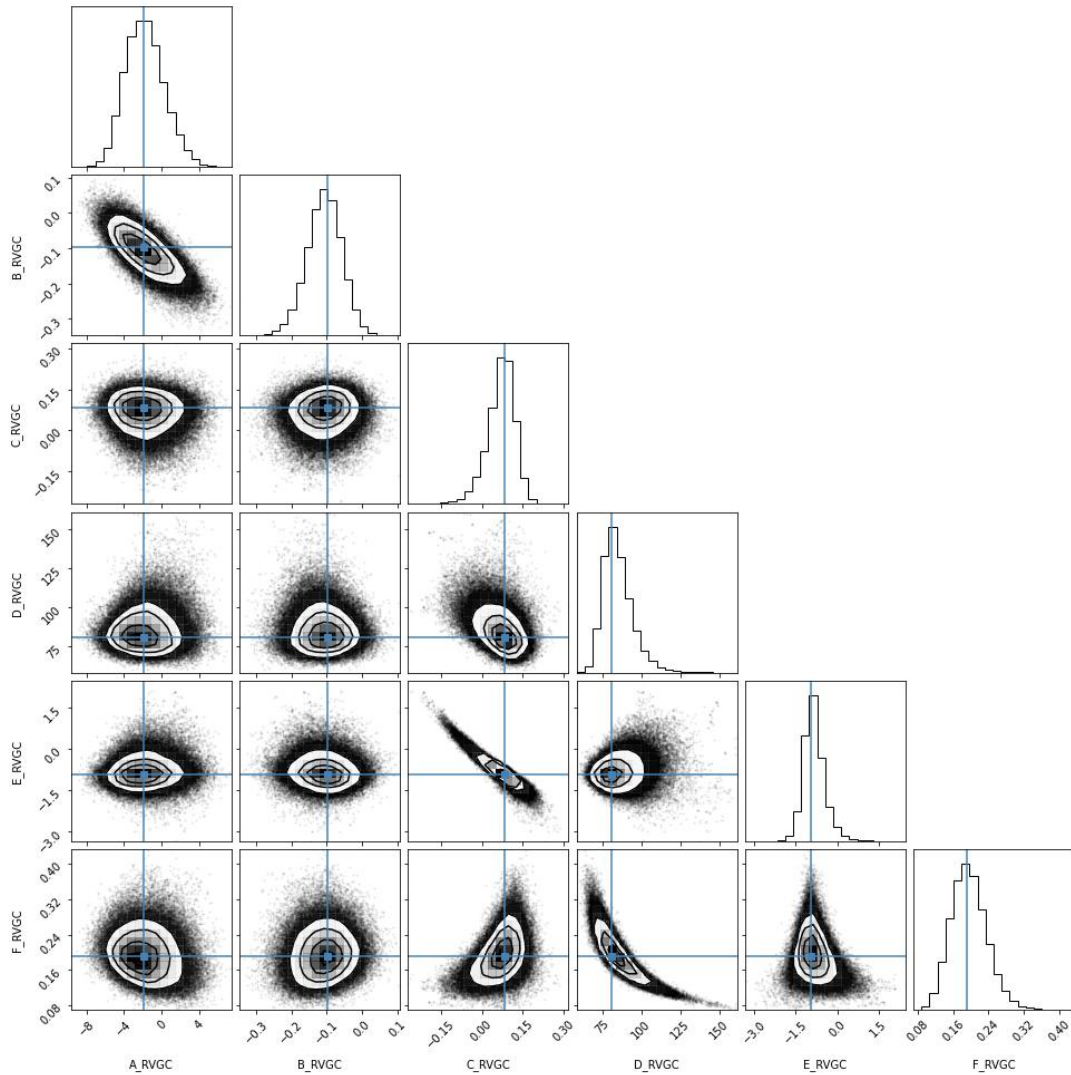


Fig. B.1. Corner plot showing the posterior distributions of the coefficients for the RV map in the Galactic bulge. These coefficients were derived using MCMC sampling to fit an analytical equation to the updated dataset. The well defined Gaussian shapes in the 2D distributions indicate a robust determination of the coefficients.

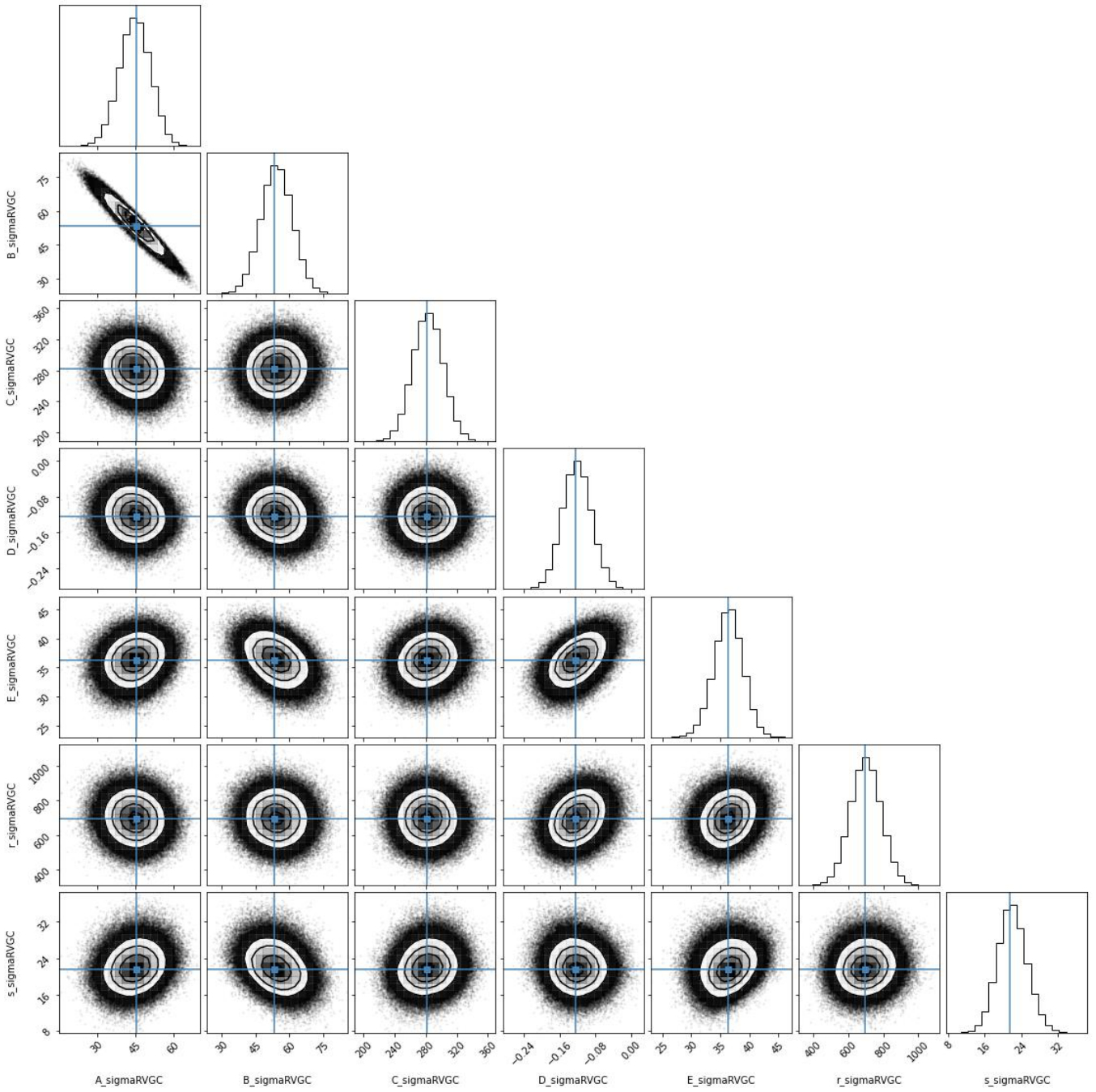


Fig. B.2. Corner plot showing the posterior distributions of the coefficients for the σ_{RV} map in the Galactic bulge. Similar to the previous figure, these distributions represent the robust determination of parameters used to model the σ_{RV} profile as we notice, each parameter distribution is well represented as a gaussian.

Appendix C: Older vs new maps comparison.

To highlight the impact of the new MUSE observations and the updated model fits, Figures C.1 and C.2 present difference maps comparing our results with those of Z14. These maps show the residual in mean RV and velocity dispersion (σ_{RV}) calculated as Z14 minus the updated values. Only the positions of the new data points (for instance, New MUSE, V18 and APOGEE data) are overlaid, highlighting the regions where our measurements provide improved constraints over the previous dataset.

The comparison shows that most differences are concentrated near the Galactic plane, within $|b| < 2^\circ$, where the new data offer improved spatial coverage. Mean RV differences are generally moderate, mostly under 15 km/s, and correspond to asymmetries in the original Z14 maps that are now corrected. In contrast, the σ_{RV} differences are pronounced, highlighting a reshaped morphology of the central velocity dispersion peak. Notably, the updated map removes the wing-like extensions seen in Z14, resulting in a more symmetric and regular structure that better reflects the distribution of the new measurements

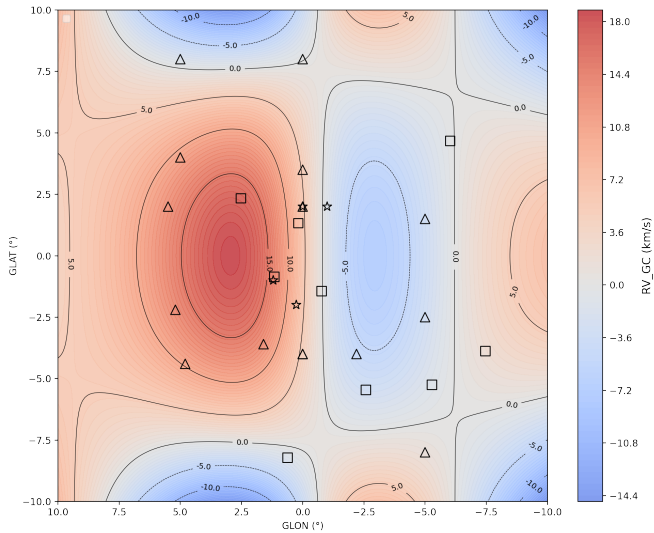


Fig. C.1. Map of the difference in mean RV between the previous Z14 map and the new one presented here (Z14 – New). The markers follow the same convention as in Fig. 1, but we only show the positions of the new data to highlight the regions where the updated map is better constrained. The new mean RV map is more symmetric and smoother than that of Z14, the asymmetry in the difference map reflects that. The largest differences appear within the inner 2° near the Galactic plane, where most of the new data are located.

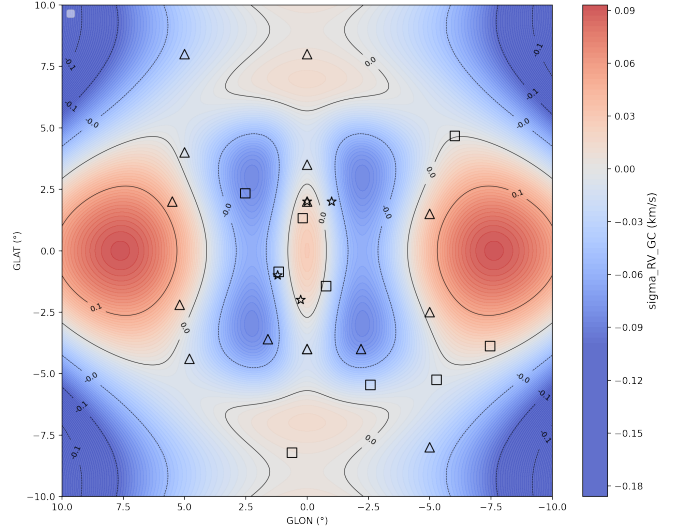


Fig. C.2. Map of the difference in σ_{RV} between the previous Z14 map and the updated version presented here (Z14 – New). The new σ_{RV} map shows more significant differences near the Galactic plane, where the additional data have smoothed the central peak and modified the intermediate contours toward a boxier morphology without the "wing-like" shape.